C. R. Mecanique 339 (2011) 655–665

Contents lists available at ScienceDirect

Comptes Rendus Mecanique

www.sciencedirect.com

Aspect ratio effects on three-dimensional incompressible flow in a two-sided non-facing lid-driven parallelepiped cavity

Fakher Oueslati *, Brahim Ben Beya, Taieb Lili

Laboratoire de mécanique des fluides, Faculté des sciences de Tunis, Département de physique, 2092 El Manar 2, Tunis, Tunisia

ARTICLE INFO

Article history:
Received 10 May 2011
Accepted after revision 16 June 2011
Available online 23 July 2011

Keywords:
Fluid mechanics
Aspect ratio
3D lid-driven cavity
Unsteady flow
Bifurcation

ABSTRACT

A numerical study of the three-dimensional fluid flow has been carried out to determine the effects of the transverse aspect ratio, A_y, on the flow structure in two-sided non-facing lid-driven cavities. The flow is complex, unstable and can undergo bifurcation. The numerical method is based on the finite volume method and multigrid acceleration. Computations have been investigated for several Reynolds numbers and various aspect ratio values. At a fixed Reynolds number, $Re = 500$, the three-dimensional flow characteristics are analyzed considering four transverse aspect ratios, $A_y = 1, 0.75, 0.5$ and 0.25. It is observed that the transition to the unsteady regime follows the classical scheme of a Hopf bifurcation. An analysis of the flow evolution shows that, at $A_y = 0.75$, the flow bifurcates to a periodic regime at ($Re = 600$) with a frequency $f = 0.093$ less than the predicted value in the cubical cavity. A correlation is established when $A_y = 0.5$ and gives the critical Reynolds number value. At $A_y = 0.25$, the periodic regime occurs at high Re value beyond 3500, after which the flow becomes chaotic. It is shown that, when increasing A_y over the unit, the flow in the cavity exhibits a complex behavior. The kinetic energy transmission from the driven walls to the cavity center is reduced at low A_y values.

1. Introduction

Research concerning the physical model of lid-driven cavity (LDC) flows is an area of continuing interest and was regarded as a benchmark study in some literature works. The interest is justified by the fact that its flow configuration is relevant to many industrial applications such as boundary layers and vortex of different size with various instabilities. However, despite the simplicity of the geometry, the LDC flow exhibits a number of interesting physical features such as complex instabilities, transitions, bifurcations and turbulence.

By far, the most studied configuration is that of two-dimensional one-sided LDC flow set up by constant speed motion of a single wall [1,2]. A recent work has been carried out by Lin et al. [3] who applied the multirelaxation time lattice Boltzmann model to compute two-dimensional LDC flows at three aspect ratio values 1, 1.5 and 4, and for different Reynolds numbers from 100 to 7500. They found steady solutions for square cavity flows, whereas, at the aspect ratios 1.5 and 4 unsteady solutions prevail at $Re = 7500$ where periodic flow exists manifested by the rapid changes of the shapes and locations of the corner vortices.

While some LDC flow phenomena have revealed 2D solutions, many subtleties of third dimensionality are missing. The recent progress in numerical analysis and computer hardware has made it possible to investigate 3D LDC flow simulations [4,5]. Ding et al. [6] discussed the effectiveness of using the local multiquadric differential quadrature method to study the

* Corresponding author.
E-mail address: fakher.oueslati@gmail.com (F. Oueslati).

1631-0721/$ – see front matter
doi:10.1016/j.crme.2011.06.002

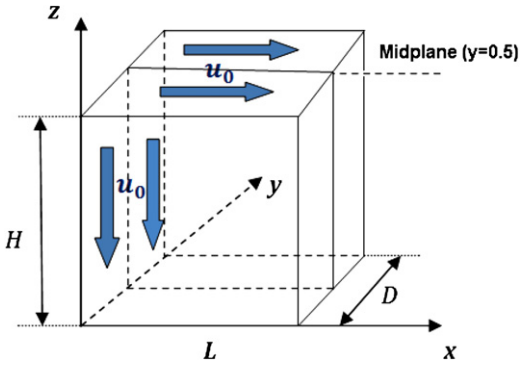

Fig. 1. Geometric description of the two-sided non-facing lid driven cavity flow.

three-dimensional LDC flow. Albensoeder et al. [7] extended the work of Botella and Peyret [2] and studied numerically the three-dimensional flow in a one sided lid-driven cavity.

Migeon et al. [8] considered the 3D LDC flow in which one wall moves with uniform velocity. The authors examined the flow spanwise structures in order to prove its three-dimensionality for a Reynolds number of 1000. In addition, a numerical study has been conducted to reveal the existence of only one corner-vortex on each end-wall.

Further studies in the literature are concerned with the appearance of bifurcations caused by Taylor–Görtler–Like instabilities (TGL). Koseff and Street [9] observed local TGL vortices over the span of the cavity with spanwise aspect ratios 1, 2 and 3. Chicheportiche et al. [10] analyzed the first bifurcation of a three-dimensional lid-driven cavity flow characterized by the TGL instabilities by a global linear stability analysis and a direct numerical simulation. Peng et al. [11] considered a two-dimensional LDC flow to study the transition from laminar to chaotic regime via Hopf bifurcations.

Regarding flow instabilities, the classical one-sided LDC flow has been extended to two-sided driven problem. In fact, when two facing walls move in parallel or anti-parallel horizontal directions the flow shows different behavior. In particular, Albensoeder et al. [12] investigated the linear stability of the 2D incompressible flow of two symmetric counter-rotating vortices in a two-sided LDC where the flow is driven by two facing walls. They found that the centrifugal instability when both vortices are distant merges smoothly to an instability in which flow deceleration and straining of the vortex cores are the determining factors. Not long ago, a new kind of 2D driven cavity in which the flow is driven by two sides non-facing walls has been computed by Wahba [13] for the first time. He extended the work for the case of four-sided LDC and established the critical *Re* number and bifurcation diagrams according to the steady and stable flow. He found that, at low Reynolds numbers, the resulting flow field is symmetric with respect to one of the cavity diagonals for the two-sided driven cavity, while it is symmetric with respect to both cavity diagonals for the four-sided driven cavity.

As an extension of Wahba's work [13], for the three-dimensional configuration, the two-sided non-facing lid (3D-TSNFL) driven cavity was performed by Ben Beya et al. [14] for the cubic case. The effects of aspect ratio on the 3D-TSNFL are not yet analyzed and the purpose of the current study is to address this issue. In this respect, the main objectives of this study are to reveal the flow patterns, the three-dimensionality of the flow and to analyze unsteadiness phenomena.

2. Physical modeling

The configuration of the three-dimensional parallelepiped enclosure, of width L, height H and depth D is sketched in Fig. 1. The cavity has a span-wise aspect ratio $A_y = \frac{D}{H}$ and a longitudinal one defined by $A_x = \frac{L}{H}$ and filled with an incompressible flow of a Newtonian fluid with constant viscosity and constant density. The flow is driven by the top wall to right and by the left vertical wall moving down with constant velocity u_0. The scales H, u_0, $p_0 = \frac{1}{2}\rho_0 u_0^2$, and $t_0 = \frac{H}{u_0}$ are used for the dimensionalization of the coordinate space $x_i = (x, y, z)$, velocity $u_i = (u, v, w)$, pressure p, and time t, respectively. The 3D-TSNFL driven fluid flow inside the enclosure obeys the Navier–Stokes equations that lead, in their dimensionless form:

$$\frac{\partial u_i}{\partial x_i} = 0 \tag{1}$$

$$\frac{\partial u_i}{\partial t} + \frac{\partial}{\partial x_j}(u_i u_j) = -\frac{\partial p}{\partial x_i} + \frac{1}{Re}\frac{\partial u_i}{\partial x_j \partial x_j} \tag{2}$$

The Reynolds number *Re* is defined by $Re = \frac{u_0 H}{\nu}$.

According to the geometric model presented in Fig. 1, the velocity boundary conditions are:

- At $z = 1$: (moving wall) $u = 1$, $v = 0$ and $w = 0$;
- At $x = 0$: (moving wall) $u = v = 0$, and $w = -1$;
- At $x = 1$, $y = 0$, $y = A_y$ and $z = 0$; $u = v = w = 0$.

Table 1
Minimum and maximum velocity components u and v on the centerline of the three-dimensional square cavity for different *Re* compared with those of Ding et al. [6].

Re	Ref. grid	$u_{\min}$	$z_{\min}$	$w_{\min}$	$x_{\min}$
100	Present work (48^3)	−0.21361	0.47702	−0.24971	0.81026
100	Ref. [6] (41^3)	−0.205	0.48	−0.246	0.80
400	Present work (48^3)	−0.22979	0.22433	−0.37685	0.87127
400	Ref. [6] (41^3)	−0.231	0.24	−0.371	0.88
1000	Present work (48^3)	−0.27447	0.12162	−0.42946	0.90410
1000	Ref. [6] (41^3)	−0.258	0.12	−0.414	0.92

3. Numerical procedure

The dimensionless Navier–Stokes equations (1) and (2) were numerically solved using the following numerical methodology. The time derivative in the momentum equations is performed by an Euler backward second-order implicit scheme. Linear terms are evaluated implicitly, while the non-linear terms are explicitly evaluated by means of an Adams–Bashforth extrapolation. We have chosen a projection method [15] in order to avoid the difficulty that the strong velocity–pressure coupling present in the continuity and the momentum equations bring forward. The momentum equations for a provisional velocity field that may not be divergent are solved at each time step. A Poisson equation with homogeneous boundary conditions is then solved and leads to update pressure and free divergence velocity fields. We have also implemented a finite volume method on a staggered grid system in order to discretize the system of equations to be solved. The QUICK scheme of Hayase et al. [16] is employed to minimize the numerical diffusion for the advective terms. Except the Poisson equation which is solved using an accelerated full multigrid method (FMG) [17], the discretized equations are solved using the red and black points successive over-relaxation RBPSOR method [18] with optimum relaxation factors. Finally, the convergence of the numerical 3D velocity field is established at each time step by controlling the L_2-residuals norm of all equations to be solved by setting its variation to less than 10^{-8}. In order to secure the steady state conditions, the following criterion has to be satisfied:

$$\sqrt{\sum_{i,j,k}\left(x^n_{i,j,k} - x^{n-1}_{i,j,k}\right)^2} < 10^{-8}$$

Here the superscript n indicates the iteration number and the subscript sequence (i, j, k) represents the space coordinates x, y and z.

4. Results and discussion

4.1. Test case

Simulations were performed by using our three-dimensional finite volume code "NASIM" [14] for the test case of a 3D lid-driven cubic cavity and validated with respect to Albensoeder et al. [7] works. For further validation, we compared the present solutions corresponding to the test case with those of Ding et al. [6]. They simulated the flow in a cubic lid-driven cavity ($A_y = 1$) applying the local multiquadric differential quadrature method. Our numerical simulations were carried out using our code in the case of a single-side lid-driven cubic cavity for different Reynolds. We have chosen to use a non-uniform staggered grid of 48^3 nodes refined near the walls [14]. In fact, the selected mesh size provides a good compromise between accuracy and CPU time in the range of Reynolds numbers to be investigated. In Table 1 are listed the extrema of the u- and w-velocity components as well as their locations and compared with the results of Ding et al. [6] for $Re = 100, 400$ and 1000. Fig. 2 shows a comparison of u- and w-velocity profiles along the centerline of the lid-driven cubical cavity of the present work with Ref. [6] at the Reynolds numbers ($Re = 400$ and 1000). Our data as well as the centerline profiles seem to be in good agreement with the results of Ref. [6].

4.2. Aspect ratio effects on the steady 3D-TSNFL driven flow

In what follows, we will present a detailed analysis of the aspect ratio effects on the three-dimensional flows in two-sided non-facing lid-driven cavity for the steady solution obtained at $Re = 500$. For this fixed Reynolds number, four transverse aspect ratios $A_y = 1, 0.75, 0.5$ and 0.25 are considered. It is worth noting that A_x is maintained to 1 in all simulations.

In Fig. 3 are presented the u- and w-contours at the mid-plane ($y = 0.5$) of the cavity for $A_y = 1$ and 0.25. Three rolls are observed for both components: a central large clockwise/anticlockwise roll and two asymmetric clockwise/anticlockwise rolls close to the walls. The intensity of the large rolls seems to become feeble by lowering the aspect ratio from the unit to 0.25. Stream traces at the mid-plane ($y = 0.5$) at $Re = 500$ for the two aspect ratio values $A_y = 1$ and 0.25 are plotted in Fig. 4.

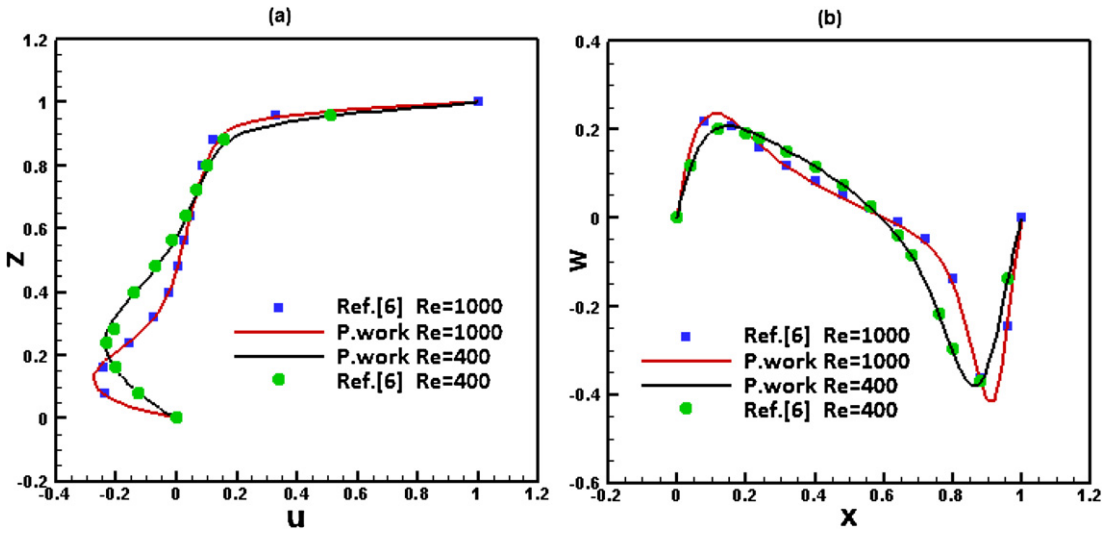

Fig. 2. Comparison of u- and w-velocity components distribution along the centerline of cubic cavity of the present work with Ref. [6] for (a) $Re = 400$ and (b) $Re = 1000$.

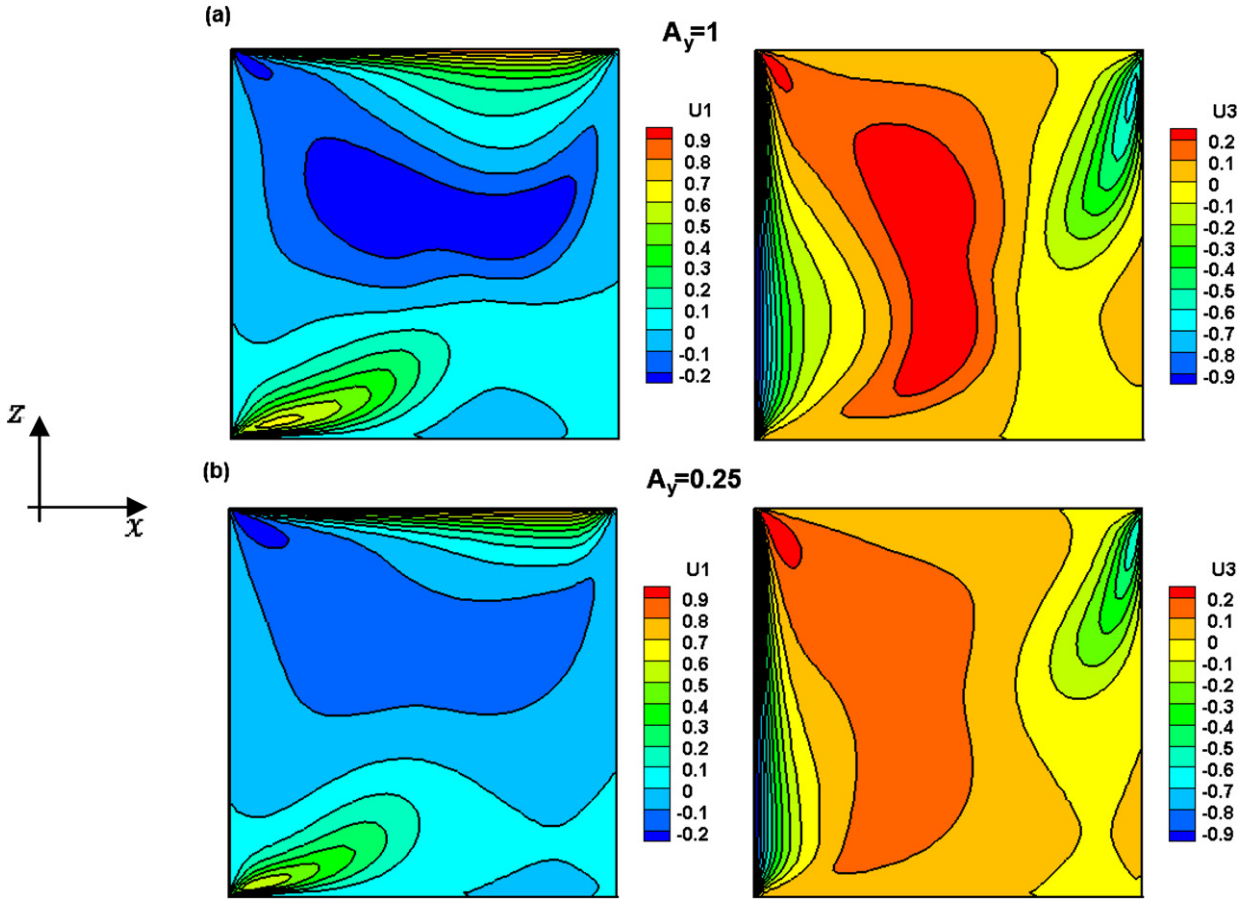

Fig. 3. Contours of u- and w-velocity components at the mid-plane ($y = 0.5$) for $Re = 500$, (a) $A_y = 1$ and (b) $A_y = 0.25$.

The flow topology is characterized by two primary and two secondary vortices symmetrically distributed by the cavity diagonal. It is clearly observed that the decrease of the aspect ratio affects the locations of the eddy centers. One can notice that the two primary vortices centers move out towards the lower left and upper right corners as the aspect ratio is

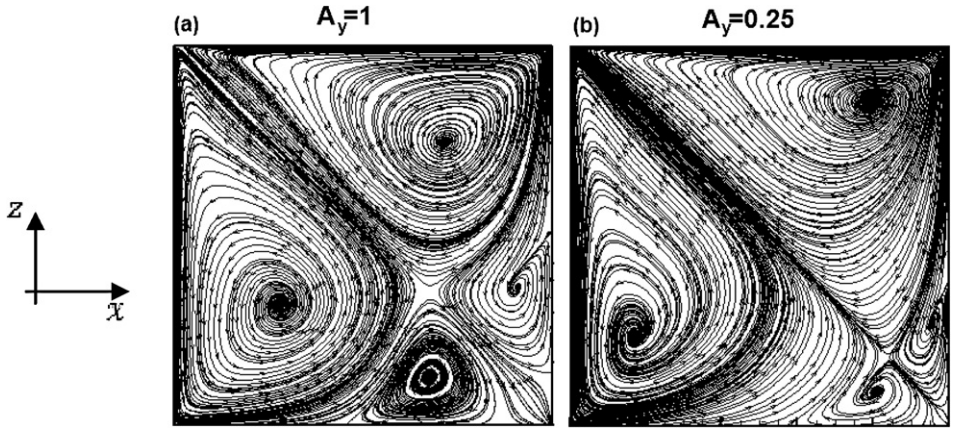

Fig. 4. Stream traces of the 3D-TSNFL driven flow at the mid-plane ($y = 0.5$) for $Re = 500$, (a) $A_y = 1$ and (b) $A_y = 0.25$.

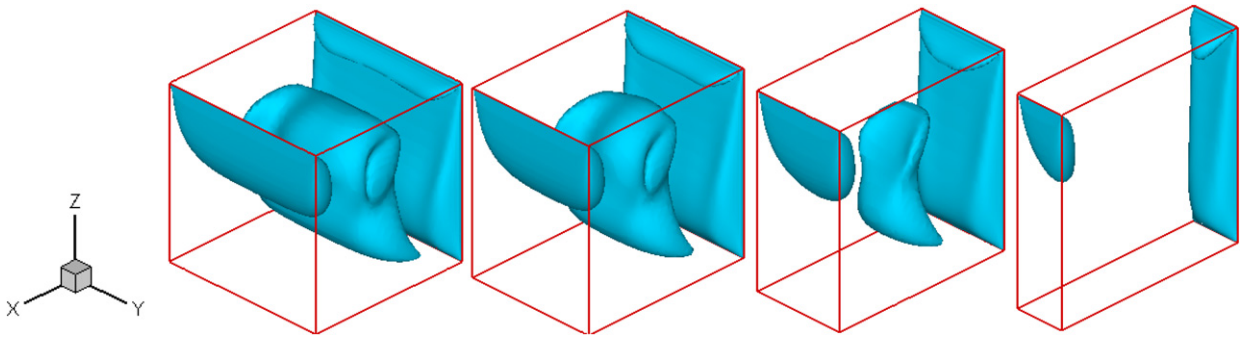

Fig. 5. Iso-surfaces of the cross-flow velocity corresponding to the value (0.20) for different aspect ratios $A_y = 1, 0.75, 0.5$ and 0.25 (from left to right) at $Re = 500$.

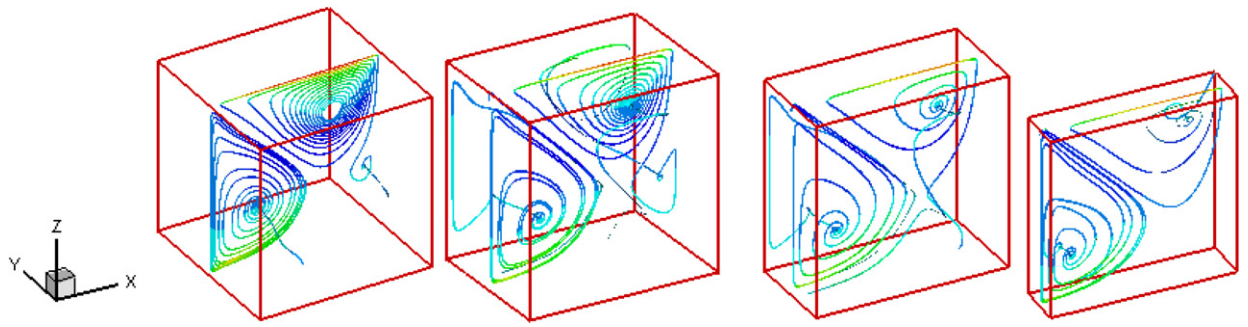

Fig. 6. The trajectory of fluid particles for different combinations of aspect ratios $A_y = 1, 0.75, 0.5$ and 0.25 (from left to right) at $Re = 500$.

decreased from $A_y = 1$ to $A_y = 0.25$. However, we can see that the two secondary vortex centers approached. Furthermore the flow remains symmetrical by the diagonal for all A_y values.

Cross-flow velocity iso-surfaces corresponding to the value (0.20) are presented in Fig. 5 for different aspect ratios $A_y = 1, 0.75, 0.5$ and 0.25 at $Re = 500$. By decreasing A_y from 1 to 0.25, we can observe, a general tendency of decrease in the iso-surfaces zone for the chosen fixed value. We should point out that the two cross flows result of the two non-facing lid-driven walls: motion of the top lid in the increasing abscissa-x and of the vertical wall in the decreasing z-direction.

Fig. 6 displays the trajectory of particles for the different envisaged cases at $Re = 500$. The introduction of a particle into the mid-plane cavity of the flow leads to the formation of two counter-rotating cells: a right and a left primary vortex. The right and left secondary vortices have not been shown by the tracks of particle as expected. The attractors seem to vanish by decreasing A_y from 1 to 0.25. The extrema values ($u_{\min}$ and $w_{\max}$) of velocity components through the cavity centerline and the corresponding locations, at various values A_y, are given in Table 2. In addition, the variation of these extrema velocity components as function of A_y, are plotted in Fig. 7. As it can be seen, $u_{\min}$ and $w_{\max}$ evolve with an opposite behavior. However, the u- and w-velocity components profiles at the mid-plane ($y = 0.5$) that are displayed in

Table 2
Extrema variation of u- and w-velocity components as function of the transverse aspect ratio A_y and the corresponding locations at the mid-plane ($y = 0.5$) for $Re = 500$.

A_y	u_{min}	z_{min}	w_{max}	x_{max}
1	−0.26344	0.57626	0.26344	0.42373
0.75	−0.25016	0.57626	0.25012	0.42373
0.5	−0.23250	0.57626	0.23243	0.43273
0.25	−0.15730	0.63558	0.15726	0.36441

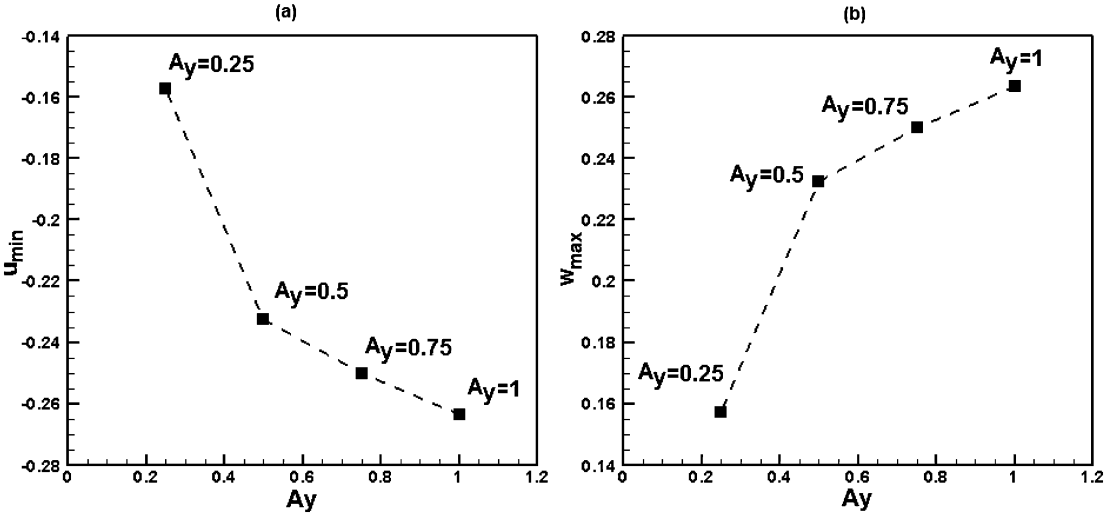

Fig. 7. Variations of the extrema of velocity components through the cavity centerline as function of the transverse aspect ratio A_y at the steady solution $Re = 500$, (a) u_{min} and (b) w_{max}.

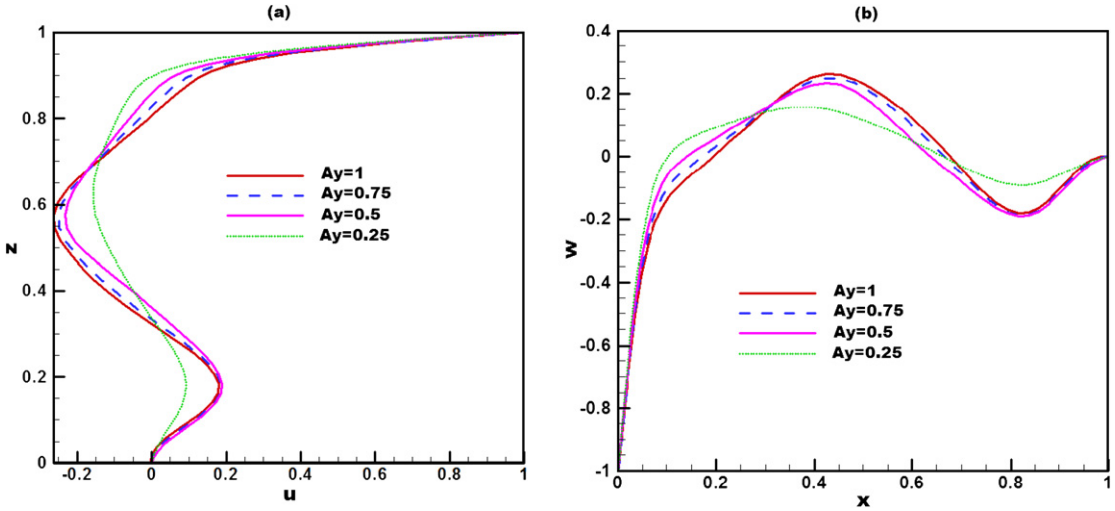

Fig. 8. Spatial variations of velocity components at $Re = 500$ for different aspect ratio values $A_y = 1, 0.75, 0.5$ and 0.25 at the mid-plane ($y = 0.5$), (a) u, and (b) w.

Fig. 8 shows a symmetric trend ($w + u = 0$) with existence of two locations $z = 0.7$ and $x = 0.3$ respectively, where u and w remain fixed for all aspect ratios.

4.3. Periodic solutions at various aspect ratios

Concerning the transition of the 3D-TSNFL driven flow, we found that this one became unsteady and we observed a periodic regime when Re exceeded a threshold value. For instance, at $Re = 600$, a periodic solution has been found for two configurations corresponding to $A_y = 1$ and 0.75.

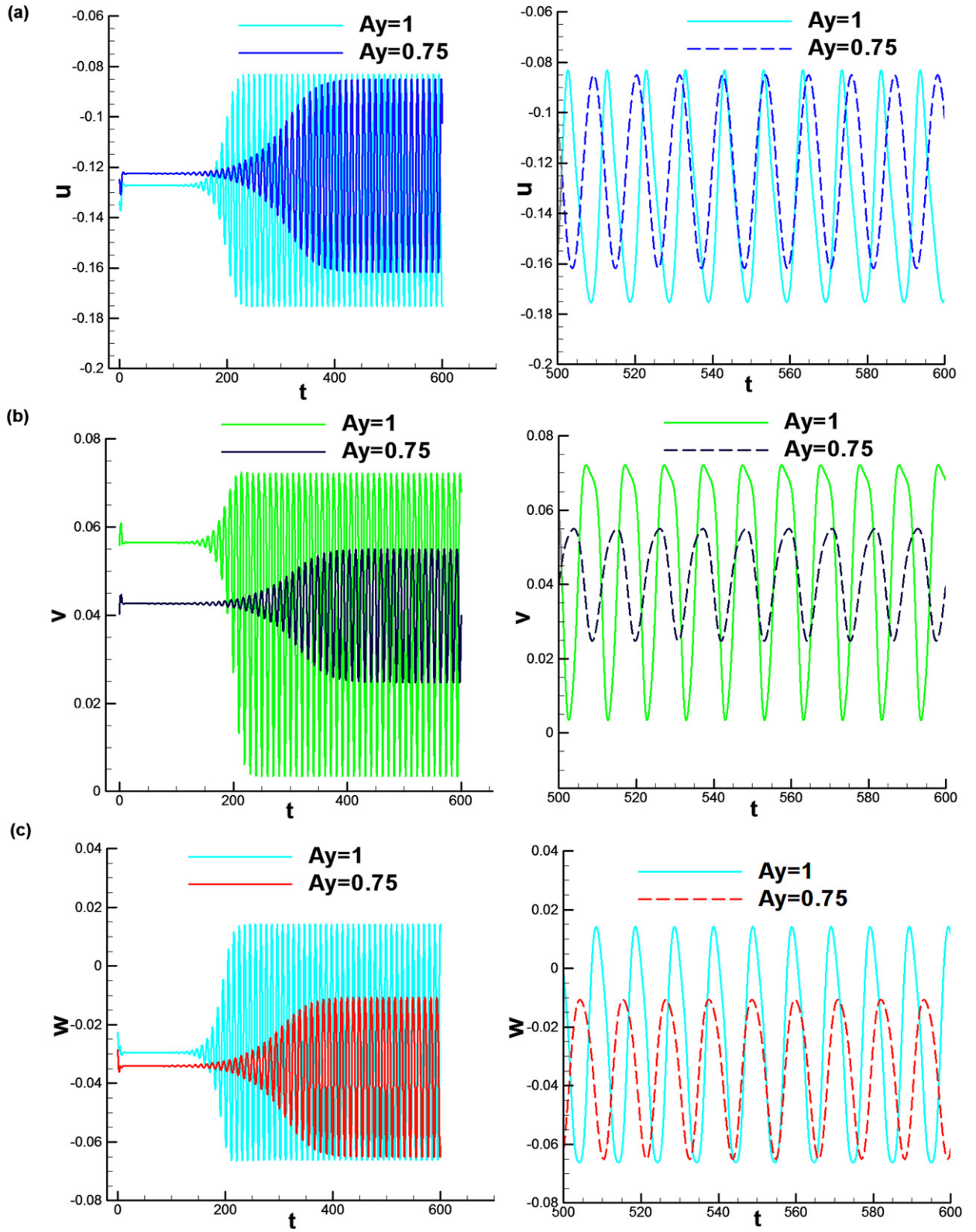

Fig. 9. Temporal variations of velocity components at the monitoring point $C_1(0.25, 0.5, 0.25)$ for different time intervals at the Reynolds number $Re = 600$, (a) u, (b) v and (c) w.

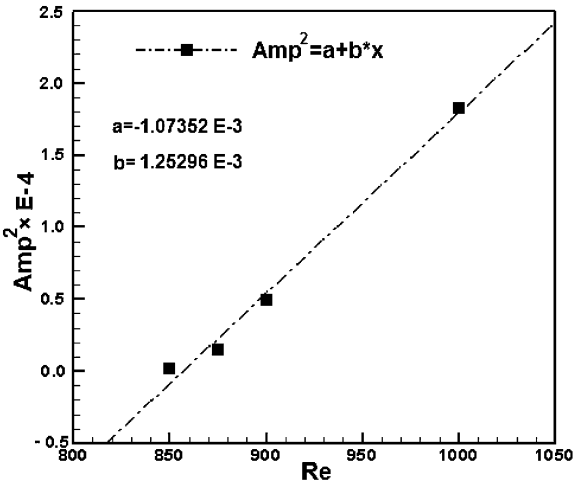

Fig. 10. Square u-velocity component magnitude fluctuations against the Reynolds number for ($A_y = 0.5$).

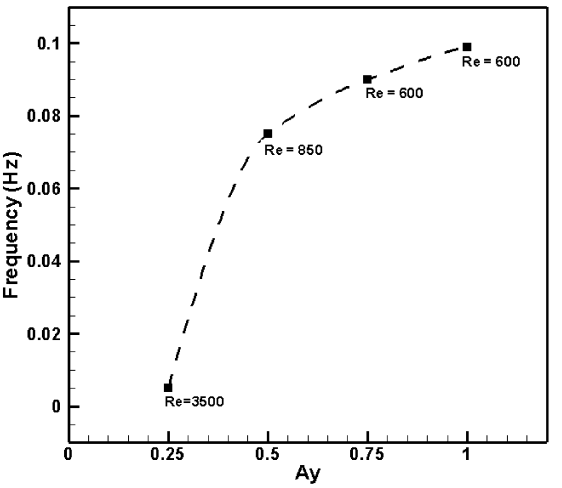

Fig. 11. Identification of periodic regimes for the corresponding aspect ratios $A_y = 1, 0.75, 0.5$ and 0.25.

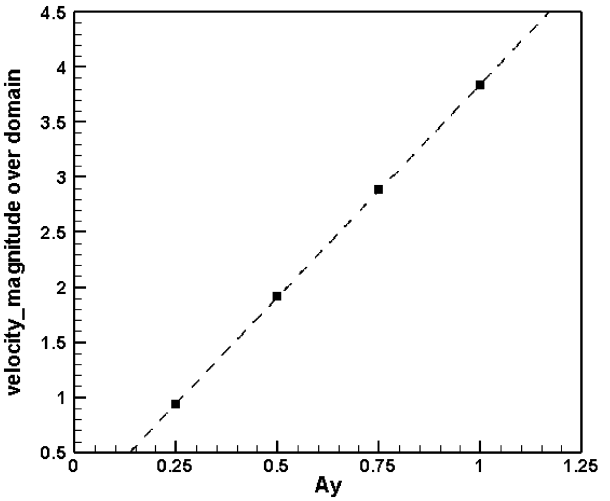

Fig. 12. Magnitude of velocity across the rectangular cavity domain as function of the aspect ratio A_y at fixed $Re = 500$.

Fig. 9 displays the periodic behavior of u-, v- and w-velocity components at the monitoring point $C_1(0.25, 0.5, 0.25)$ We can notice a decrease in the amplitude of velocity components fluctuation from the cubic cavity ($A_y = 1$) to that with $A_y = 0.75$. Furthermore, analysis of the frequency spectrum in $A_y = 0.75$ indicates a frequency fluctuation equal to 0.0928. This value is less than the frequency $f = 0.1015$ found in the test case (Ref. [14]). It is worth noting that all velocity components oscillate with the same frequency.

According to $A_y = 0.5$, we have identified a Hopf bifurcation (Ref. [19]) leading to periodic solutions around a Reynolds number of $Re = 850$. Using the same method presented in the previous work (Ref. [14]), the critical Reynolds number corresponding to the Hopf bifurcation is performed to be $Re_c = 817 \pm 2\%$ which is greater than $Re_c = 540 \pm 2\%$ relative to the test case (see Fig. 10).

In Fig. 11 we have reported the Re values corresponding to periodic solutions at different A_y. In fact, by making the vertical walls closer, the onset of unsteadiness is significantly delayed. It is important to note that at the aspect ratio $A_y = 0.25$, the Reynolds number should be increased to a value close to 3500 requiring over 600 dimensionless time steps to reach the unsteady regime.

In fact, the vortices such as those of Taylor Görtler which are responsible for the appearance of the unsteadiness and consequently producing bifurcations become less predominant when the confined cavity loses volume.

The influence of the aspect ratio on the velocity magnitude over the whole cavity domain can be also observed in Fig. 12. This figure reflects a net increase in the flow intensity through the entire cavity as A_y increases.

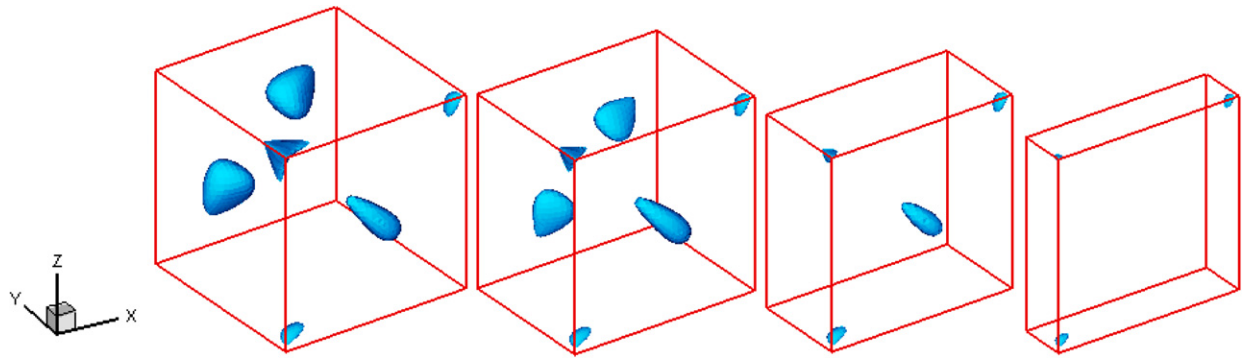

Fig. 13. Iso-surfaces of the transverse velocity component v for the specific value (-0.06383) for different aspect ratio values $A_y = 1, 0.75, 0.5$ and 0.25 (from left to right) at $Re = 500$.

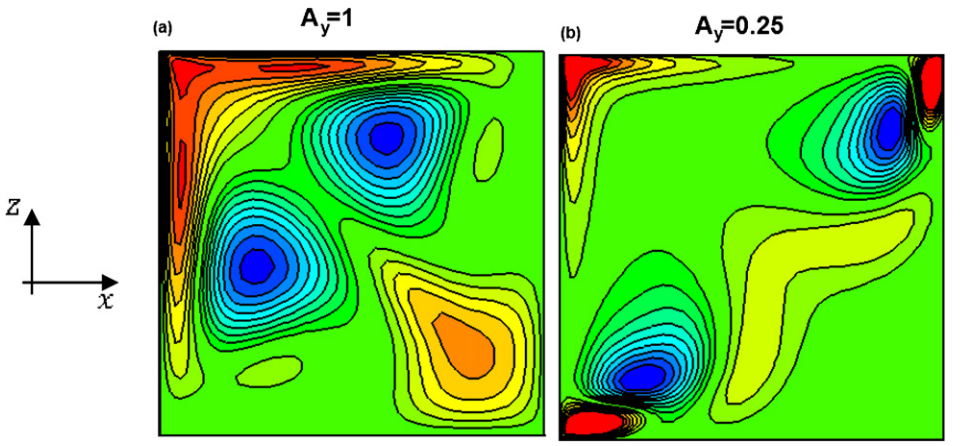

Fig. 14. Iso-contours of the transverse velocity component v at the mid-plane $(y = 0.5)$ for the steady case $(Re = 500)$, (a) $A_y = 1$ and (b) $A_y = 0.25$.

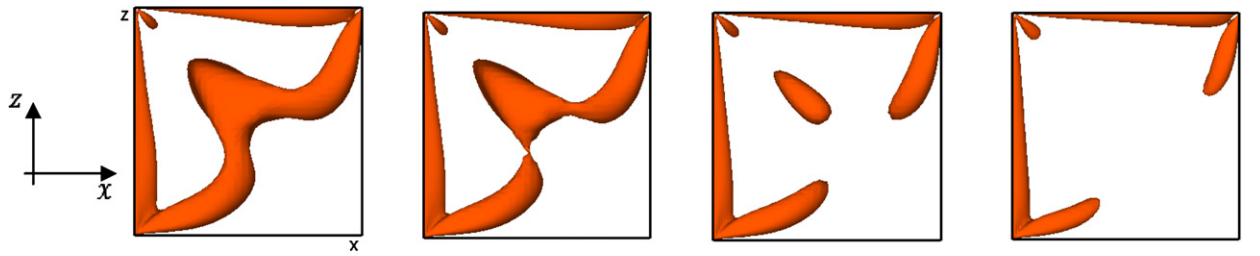

Fig. 15. Iso-surfaces of the kinetic energy $(E_c = 0.4)$ for various values of transverse aspect ratios $A_y = 1, 0.75, 0.5$ and 0.25 at $Re = 500$.

4.4. On the three-dimensionality effects

In order to analyze the influence of aspect ratio on the three-dimensionality nature of the flow, the iso-surface of the spanwise velocity component v for the specific value (-0.06383) and a fixed $Re = 500$ is shown in Fig. 13. From this figure, we can see that the three-dimensional effects begin to decrease gradually until they disappear. This means that the three-dimensional configuration seems to move to a two-dimensional configuration especially for the small aspect ratio $A_y = 0.25$.

The iso-contours of the v-velocity component (Fig. 14) with $A_y = 1$ and 0.25 confirm the important 3D effects discussed in the previous figure. In addition, a net symmetry of the flow pattern by the cavity diagonal is also observed. Fig. 15 displays the iso-surfaces of the kinetic energy defined by $E_c = \frac{1}{2}(|u|^2 + |v|^2 + |w|^2)$ corresponding to the value $(E_c = 0.04)$ for various aspect ratios A_y at $Re = 500$. By making the spanwise vertical walls closer, the kinetic energy is less transmitted from the driven walls to the cavity center. This may be explained by the fact that the decrease of the aspect ratio has led to a decrease of the surface contact. Hence, the driven fluid particles become fewer and cause a net decrease of the kinetic energy. We have also adopted another way to better analyze the 3D effects by visualizing the tensor gradient velocity $(\frac{\partial v}{\partial y})$

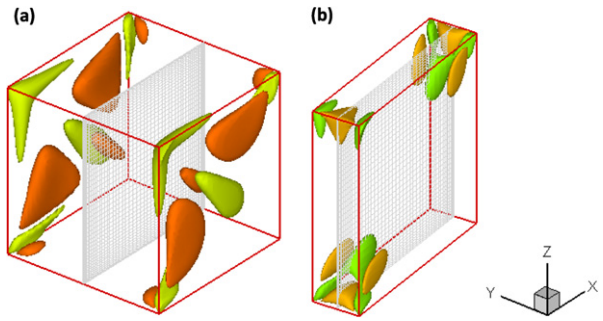

Fig. 16. Iso-surfaces of the tensor gradient velocity component ($\frac{\partial v}{\partial y}$) (contour levels range between -4.5 and 1.5) at the steady solution for $Re = 500$, (a) $A_y = 1$ and (b) $A_y = 0.25$.

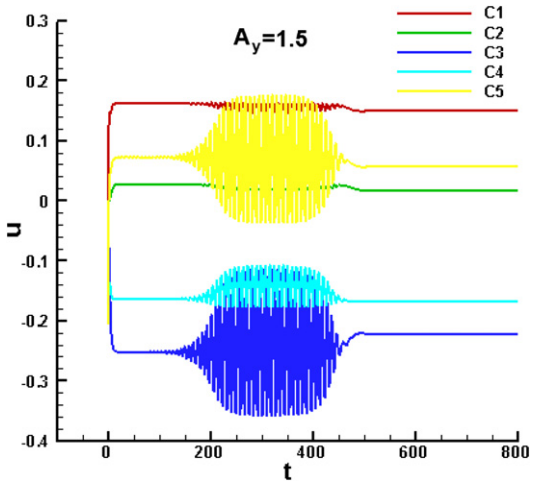

Fig. 17. Time evolution of the u-velocity component at five monitoring points C_1, C_2, C_3, C_4 and C_5 for the aspect ratio value $A_y = 1.5$ at $Re = 500$.

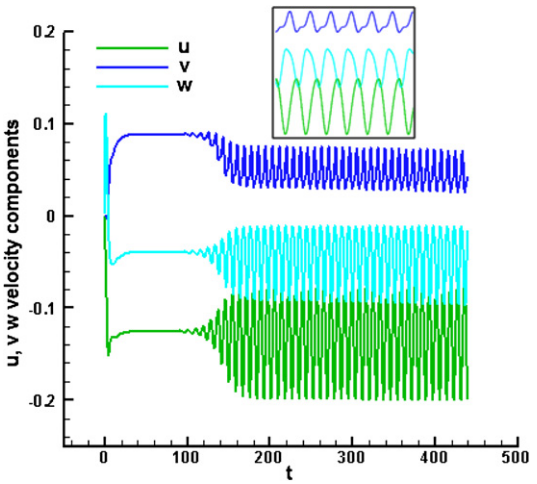

Fig. 18. Periodic behavior of the 3D-TSNFL driven flow at $Re = 500$ of u-, v-, w-velocity components at the monitoring point $C_1(0.25, 0.5, 0.25)$ for $A_y = 2$.

for $A_y = 1$ and 0.25 (Fig. 16). These results indicate that the transverse tensor gradient velocity is very dependent of the aspect ratio.

4.5. Flow patterns for A_y over the unit

In this section we will present the results for A_y over the unit. Two configurations were used in this study relatively to the aspect ratios $A_y = 1.5$ and 2. The simulations were performed using a mesh of $(48 \times 80 \times 48)$ nodes, a dimensionless time of about 600 and a time step $\Delta t = 5 \times 10^{-3}$.

The present computational simulation shows that the 3D-TSNFL driven flow at the aspect ratio $A_y = 1.5$ undergoes a developed unsteady state at the Reynolds number $Re = 500$. The time signal of the u-velocity component for $A_y = 1.5$ and at five monitoring points is presented in Fig. 17. For this figure, the time dependent solution of the 3D-TSNFL driven flow exhibits a periodic behavior during a limited temporal interval outside of which the flow remains steady. At this stage $(A_y = 1.5)$ it seems that the flow migrates to a complex behavior and further analysis should be made to get a valid conclusion. In fact, as the aspect ratio increases $(A_y = 2)$ and for the same $Re = 500$, a more maintained periodic solution is reached with a frequency equal to 0.116 (Fig. 18).

5. Conclusion

The present study is aimed to confirm the A_y effects in the 3D-TSNFL driven parallelepiped cavities using a finite volume code with the help of a full multigrid acceleration.

The performance of the present model is demonstrated by a benchmark problem dealing with the cubic cavity (test case).

Firstly, the structure of the flow patterns has been described in the steady case at $Re = 500$. Analysis of the flow topology at the mid-plane $(y = 0.5)$ demonstrates the presence of two primary and secondary vortices which remain symmetrical by

the diagonal for all A_y values. Furthermore, maxima of w-velocity component strengthens with the increasing value of A_y, whereas the strength of minima u-velocity component weakens with increasing A_y.

When Re exceeds a threshold value the flow exhibits a periodic state. In particular, a critical Re number of $817 \pm 2\%$ computed for $A_y = 0.5$ was found to be greater than the one predicted in the test case. Moreover, it is found that by making the vertical walls closer, the onset of unsteadiness is significantly delayed.

It is observed that, for small values of A_y, the kinetic energy is less transmitted from the driven walls to the cavity center. The 3D effects are also reflected in the iso-surfaces of the transverse velocity component and those of the tensor gradient velocity.

Finally, when A_y attains the value greater than unit, the flow migrates to a complex behavior which needs to be more clarified with further studies.

References

[1] E. Erturk, Discussions on driven cavity flow, Internat. J. Numer. Methods Fluids (2009) 275–294.
[2] O. Botella, R. Peyret, Benchmark spectral results on the lid-driven cavity flow, Comput. & Fluids 27 (1998) 421–433.
[3] L. Lin, Yi-Cheng Chen, Chao-An Lin, Multi relaxation time lattice Boltzmann simulations of deep lid driven cavity flows at different aspect ratios, Comput. & Fluids (2011).
[4] K.L. Wong, A.J. Baker, A 3D incompressible Navier–Stokes velocity-vorticity weak form finite element algorithm, Internat. J. Numer. Methods Fluids 38 (2002) 99–123.
[5] Q.T. Li, T. Cheng, T.T.H. Tsang, Transient solutions for three-dimensional lid-driven cavity flows by a least-squares finite element method, Internat. J. Numer. Methods Fluids 21 (1995) 413–432.
[6] H. Ding, C. Shu, K.S. Yeo, D. Xu, Numerical computation of three-dimensional incompressible viscous flows in the primitive variable form by local multiquadric differential quadrature method, Comput. Methods Appl. Mech. Engrg. 195 (2006) 516–533.
[7] S. Albensoeder, H.C. Kuhlmann, Accurate three-dimensional lid-driven cavity flow, J. Comput. Phys. 206 (2005) 536–558.
[8] C. Migeon, G. Pineau, A. Texier, Three-dimensionality development inside standard parallelepipedic lid-driven cavities at $Re = 1000$, J. Fluids Struct. 17 (2003) 717–738.
[9] J.R. Koseff, R.L. Street, Visualization studies of a shear driven three-dimensional recirculating flow, ASME J. Fluid Engrg. 33 (1984) 594–602.
[10] J. Chicheportiche, X. Merle, X. Gloerfelt, J.-C. Robinet, Direct numerical simulation and global stability analysis of three-dimensional instabilities in a lid-driven cavity, C. R. Mecanique 336 (2008).
[11] Y. Peng, Yuo-Hsien Shiau, Robert R. Hwang, Transition in a 2-D lid-driven cavity flow, Comput. & Fluids 32 (2003) 337–352.
[12] S. Albensoeder, H.C. Kuhlmann, Three-dimensional instability of two counter-rotating vortices in a rectangular cavity driven by parallel wall motion, Europ. J. Mech. B/Fluids 21 (2002) 307–316.
[13] E.M. Wahba, Multiplicity of states for two-sided and four-sided lid driven cavity flows, Comput. & Fluids 38 (2008) 247–253.
[14] B. Ben Beya, Taieb Lili, Three-dimensional incompressible flow in a two-sided non-facing lid-driven cubical cavity, C. R. Mecanique 336 (2008) 863–872.
[15] D.L. Brown, R. Cortez, M.L. Minion, Accurate projection methods for the incompressible Navier–Stokes equations, J. Comput. Phys. 168 (2001) 464–499.
[16] T. Hayase, J.A.C. Humphrey, R. Greif, A consistently formulated QUICK scheme for fast and stable convergence using finite-volume iterative calculation procedures, J. Comput. Phys. 98 (1992) 108–118.
[17] N.B. Cheikh, B. Ben Beya, T. Lili, Benchmark solution for time-dependent natural convection flows with an accelerated full-multigrid method, Numer. Heat Transfer B 52 (2007) 131–151.
[18] R. Barrett, M. Berry, T.F. Chan, et al., Templates for the Solution of Linear Systems: Building Blocks for Iterative Methods, SIAM, 1994.
[19] J. Shen, Hopf bifurcation of the unsteady regularized driven cavity flow, J. Comput. Phys. 95 (1991) 228–245.